Biogeochemistry (2011) 104:69–90
DOI 10.1007/s10533-010-9484-8

Field measurements and modeling of groundwater flow and biogeochemistry at Moses Hammock, a backbarrier island on the Georgia coast

W. P. Porubsky · S. B. Joye · W. S. Moore · K. Tuncay · C. Meile

Received: 15 April 2009 / Accepted: 31 May 2010 / Published online: 29 June 2010

Abstract A combination of field measurements, laboratory experiments and model simulations were used to characterize the groundwater biogeochemical dynamics along a shallow monitoring well transect on a coastal hammock. A switch in the redox status of the dissolved inorganic nitrogen (DIN) pool in the well at the upland/saltmarsh interface occurred over the spring-neap tidal transition: the DIN pool was dominated by nitrate during spring tide and by ammonium during neap tide. A density-dependent reaction-transport model was used to investigate the relative importance of individual processes to the observed N redox-switch. The observed N redox-switch was evaluated with regard to the roles of nitrification, denitrification, dissimilatory nitrate reduction to ammonium (DNRA), ammonium adsorption, and variations in inflowing water geochemistry between spring and neap tides. Transport was driven by measured pressure heads and process parameterizations were derived from field observations, targeted laboratory experiments, and the literature. Modeling results suggest that the variation in inflow water chemistry was the dominant driver of DIN dynamics and highlight the importance of spring-neap tide variations in the high marsh, which influences groundwater biogeochemistry at the marsh-upland transition.

Keywords Hammock groundwater · Nitrogen cycle · Upland-marsh transition · Spring-neap tide cycle · Reaction transport modeling

W. P. Porubsky · S. B. Joye (✉) · C. Meile (✉)
Department of Marine Sciences, The University of Georgia, Athens, GA 30602, USA
e-mail: mjoye@uga.edu

C. Meile
e-mail: cmeile@uga.edu

W. S. Moore
Department of Geological Sciences, The University of South Carolina, Columbia, SC 29208, USA

K. Tuncay
Department of Civil Engineering, Middle East Technical University NCC, Kalkanli, Guzelyurt TRNC, Mersin 10, Turkey

Introduction

Quantification and characterization of nutrient delivery to the coastal ocean are critical for understanding anthropogenic impacts on ecosystem dynamics and global biogeochemical cycles. Development of comprehensive nutrient budgets requires consideration of both riverine (e.g., Cotrim da Cunha et al. 2007; Nixon et al. 1996) and groundwater inputs. Globally, volumetric fresh groundwater discharge is only a fraction of riverine discharge (Burnett et al. 2003); however, in the Atlantic Ocean groundwater discharge of terrestrial freshwater mixed to some extent with seawater is estimated to be 80–160% of

freshwater river discharge (Moore 1996; Moore et al. 2008). Because coastal groundwater typically contains higher concentrations of nutrients than surface water, it can contribute significantly to nutrient budgets in estuarine (Valiela et al. 1990; Burnett et al. 2003; Kroeger and Charette 2008) and nearshore (Moore et al. 2002) systems. With coastal ecosystems under increasing pressure due to development and increased population density (Vitousek et al. 1997), insight into nutrient source and reactivity has become increasingly important. Groundwater-derived dissolved nutrients may undergo extensive transformations that affect nutrient speciation and bioavailability during transit from uplands to the coastal zone (Moore 1999). Thus, understanding the processes occurring in the subsurface freshwater–saltwater transition zones is critical for developing accurate nutrient loading estimates to the coastal ocean.

Groundwater flow from the terrestrial to the marine realm depends on pressure head gradients and on soil properties that influence hydraulic conductivity. When approaching the salinity interface, density effects become important, and tidal pumping can impact discharge to intertidal environments and estuarine receiving waters (Schultz and Ruppel 2002). Hammocks, backbarrier islands typically surrounded by saltmarshes, are common geomorphological features on the southeast coast of the United States. They constitute an environment in which all the above mentioned processes are relevant: shallow groundwater flow is driven by recharge via precipitation, and flow paths are impacted by the intrusion of saltwater, which results in inflow of saltwater at depth and discharge of fresh or brackish water where the water table intersects the marsh or creek bank in the upper portions of the aquifer. The flow pattern is also affected by sea level changes due to tidal forcing and storms. Variations in marsh inundation and flushing intensity associated with spring/neap tides can alter the elemental composition of the fluid near the intertidal-upland transition, ultimately impacting the chemical speciation and magnitude of nutrient export to tidal creeks and estuaries (Snyder et al. 2004). Hence, hammock habitats are well suited for studying the fate of nutrients in shallow groundwater traveling from the upland to the intertidal marsh and ultimately the coastal ocean.

Nitrogen is generally the limiting nutrient to primary production in marine systems. As a consequence, the magnitude and bioavailability of nitrogen inputs are important for understanding ecosystem function (Nixon et al. 1996). Numerous anthropogenic point and non-point sources of nitrogen, in particular wastewater discharge and agricultural runoff (Nixon and Pilson 1983), are primary causes of coastal eutrophication (Valiela et al. 1997; Paerl et al. 1998; Pinckney et al. 2001). Increases in the frequency of estuarine hypoxia/anoxia have been linked to higher nitrogen and organic matter delivery from developed watersheds (De Jonge et al. 1994; Paerl et al. 1998; Persky 1986). The two main forms of dissolved inorganic nitrogen (DIN) in groundwater are nitrate (NO_3^-) and ammonium (NH_4^+). Groundwater flow exposes DIN to different physico-chemical environments that can impact the chemical composition of the fluid. Ammonium can be converted to NO_3^- under oxic conditions (nitrification), combined with nitrite (NO_2^-) to produce N_2 (anaerobic ammonium oxidation, anammox) or taken up or released in the creation/breakdown of organic matter; NH_4^+ is also subject to cation exchange with the solid phase. In addition to being biologically assimilated, NO_3^- can serve as a terminal electron acceptor producing dinitrogen (N_2) (denitrification, DNF) or NH_4^+ (dissimilatory nitrate reduction to ammonium, DNRA). Thus, the speciation of the groundwater-associated inorganic nitrogen may be tightly linked to the microbial processes occurring along the transport route. Because anammox, the formation of N_2 from ammonium and nitrite, and DNF constitute nitrogen sinks by converting bioavailable N into dinitrogen gas, these processes can mitigate NO_3^- inputs and reduce eutrophication of receiving waters.

Rates and controls of microbially mediated nitrogen transformation in coastal environments have been examined previously. The influence of sulfide inhibition on nitrification in estuarine and marsh sediments has been demonstrated both in the laboratory and the field (Joye and Hollibaugh 1995; Tobias et al. 2001). Several studies have employed both field and laboratory methods to examine the regulation of DNF (Rysgaard et al. 1999; An and Joye 2001; Tobias et al. 2001), including the effects of temperature and dissolved organic carbon (DOC), sulfide or oxygen concentration (Tiedje et al. 1982; Kelly-Gerreyn et al. 2001; An and Gardner 2002; Porubsky et al. 2009).

The rates of DNRA have been the focus of several field studies investigating the fate of DIN in coastal sediments (Tobias et al. 2001; Gardner et al. 2006; Kartal et al. 2007). The abundance of electron donors and acceptors are critical factors determining the relative importance of DNRA versus DNF (Porubsky et al. 2009). The potential importance of anammox (Thamdrup and Dalsgaard 2002; Risgaard-Petersen et al. 2003) in coastal areas is unclear at present, though recent data suggests that it is of minor importance in marshes (Koop-Jakobsen and Giblin 2009). Additionally, sorption of NH_4^+ via ion exchange, a process sensitive to variations in salinity, can remove a significant portion of NH_4^+ from solution and thereby affect transport and speciation of nitrogen (Seitzinger et al. 1991; Morse and Morin 2005; Böhlke et al. 2006).

Here we assess the fate of DIN in the groundwater discharge area of a coastal marsh-upland environment at Moses Hammock (MH), located on Sapelo Island, Georgia, United States of America. Field observations in winter, spring and summer demonstrated a recurring change in the $(NO_3^- + NO_2^-)/NH_4^+$ ratio of groundwater near the upland-marsh transition zone over spring-neap tidal cycles. Motivated by field observations, targeted laboratory experiments were performed to quantify rates of key processes in the nitrogen cycle. Field and laboratory findings were integrated into a variable density reactive transport model representing a vertical 2D cross section of the upland aquifer. Model simulations were carried out for both spring and neap tide conditions to identify the processes responsible for the observed differences in DIN speciation.

Methods

Study site

MH is a small (approximately 0.08 km^2), sandy coastal hammock located on the western side of Sapelo Island, Georgia (Fig. 1). MH is bordered to the west by the Duplin River whose 11 km^2 watershed is dominated (~80%) by *Spartina alterniflora* saltmarsh and unvegetated mudflats (Pomeroy

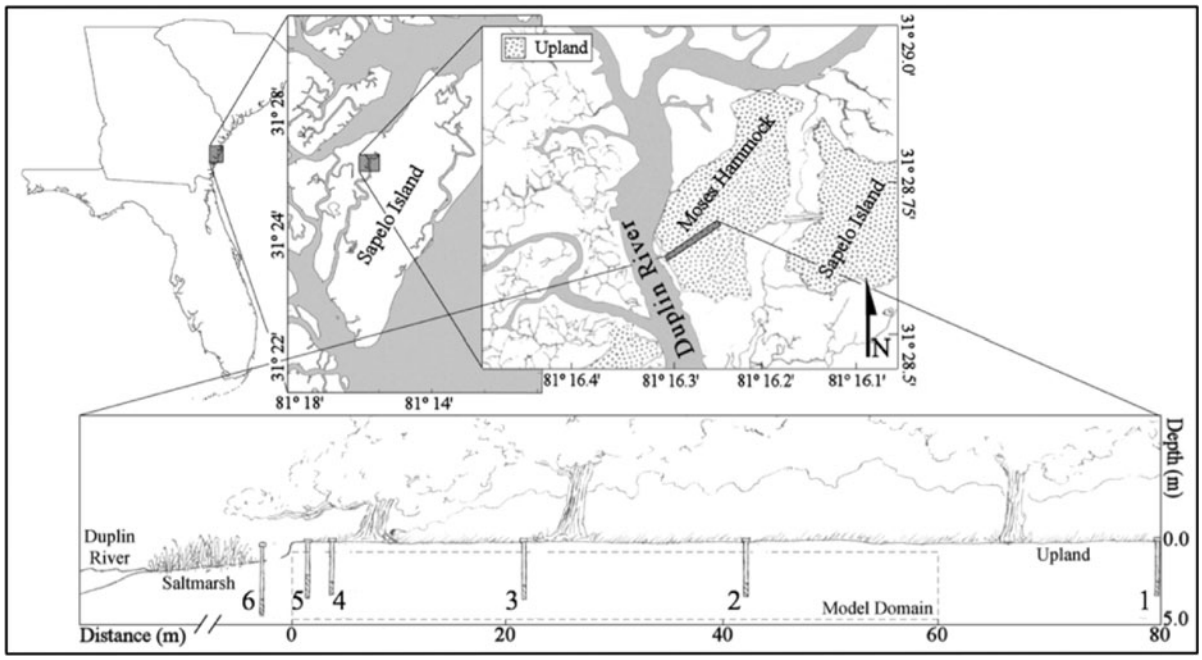

Fig. 1 Site map indicating the location of MH on the western side of Sapelo Island, Georgia. The *bottom panel* illustrates the well transect, indicating the locations of the individual wells (*1–6*). The *dashed box* delineates the model domain. Detailed screen depths and distances from the Duplin River are given in Schultz and Ruppel (2002) and Snyder et al. (2004) with the following well identification: *1* MW0208, *2* MW0214, *3* MW0203, *4* MW0202, *5* MW0201, *6* MW0217

and Wiegert 1981). The Duplin has a tidal amplitude of approximately 3.4 m for spring tide (Chalmers 1997), with a salinity, averaged over all sampling periods, of 25.7.

Aside from seasonal use as a hunting camp, MH is subjected to little anthropogenic impact. The MH upland is forested and separated from the upland of Sapelo Island by extensive *Spartina* marsh. The freshwater lens on MH is isolated from the saline aquifer underlying the island (Schultz and Ruppel 2002). A 80 m long transect of partially screened, groundwater monitoring wells (<5 m sampling depth) runs perpendicular to the Duplin River from the approximate center of MH to the saltmarsh (Schultz and Ruppel 2002; Fig. 1).

Field and laboratory methods

Well sampling

The MH well transect was sampled during low tide regularly over a 3 year period. Sample collection occurred on spring tides in April 2002, August 2003, January and June 2004; neap tide samplings occurred in April and August 2003, April, June and December 2004. Groundwater (GW) was collected for geochemical analysis using a peristaltic pump and rigid (acid-cleaned) polyethylene tubing. A galvanic dissolved oxygen probe (Orion© model no. 084260) was placed in a plastic receptacle and the groundwater was allowed to overflow it ensuring minimum atmospheric contamination of the sample. The groundwater was pumped until the temperature and dissolved oxygen measurements stabilized and then a sample (~200 ml) was collected into a gas tight bottle. Sub-samples were later dispensed for various analyses in the laboratory as described below.

A small volume of water (~1.5 ml) was collected via a plastic syringe and passed through a flow-through cell containing a flat surface combination pH/reference electrode (Sensorex® 450C). Sulfide concentration was determined via colorimetry on a 2 ml sub-sample that was filtered (National Scientific©, Target 0.2 μm pore size) and fixed in the field with zinc acetate (Cline 1969). Dissolved inorganic carbon ($DIC = H_2CO_3 + HCO_3^- + CO_3^{2-}$) was determined on a 0.2 μm filtered 2 ml aliquot that was acidified with 0.1 ml of concentrated phosphoric acid, which served to convert all the DIC to carbon dioxide (CO_2). Carbon dioxide concentrations were determined by injecting 1 ml of the headspace gas into a gas chromatograph (Shimadzu© GC-14A) fitted with a Carbosphere® column (Alltech Associates, Inc.) to separate CO_2 and CH_4, a methanizer to convert CO_2 to CH_4, and a flame ionization detector to detect CH_4 signals. Concentrations of CO_2 were determined by comparison of sample areas to the area obtained from a certified mix (10.04% CO_2 in Helium, Scott Specialty Gases©, and 10.0% CH_4 in Helium, National Welders Supply Co.©); linearity of the detector signal was confirmed over a range of diluted standards.

Approximately 30 ml of sample was filtered (0.2 μm) and stored at 4°C for subsequent determination of nutrient species (NO_2^- and $NO_3^- + NO_2^-$ ($=NO_x$)). A 5 ml aliquot of the filtered sample was transferred immediately to a 7 ml glass vial and fixed with 0.2 ml of phenol solution (9.6% phenol by volume) for determination of NH_4^+ concentration using colorimetry (Solorzano 1969). Nitrite and NO_x concentrations were determined by vanadium reduction and NO detection (Antek© 745 NO_3^-/NO_2^- reduction assembly and 7050 NO analyzer). Nitrate concentration was calculated as the difference between NO_x and NO_2^-.

For determination of reduced iron (Fe^{2+}), sulfate (SO_4^{2-}), chloride (Cl^-), and DOC concentrations, 20 ml of sample was filtered into a glass vial and acidified with 100 μl of concentrated trace metal grade nitric acid. Reduced iron was measured using standard colorimetric methods (Stookey 1970). Sulfate and Cl^- concentrations were determined by ion chromatography (Dionex© DX 500). DOC was measured using a total organic carbon analyzer (Shimadzu© TOC-5000). Acidified samples were sparged with CO_2 free air for 15 min prior to DOC measurement to remove inorganic carbon. Salinity (S) was calculated from Cl^- concentrations, $S = (35.453 \cdot 10^3 \cdot [Cl^-])/(1 + 1.80655 \cdot 35.453 \cdot 10^3 \cdot [Cl^-])$, where $[Cl^-]$ is in mmol l^{-1} (Mantyla 1987). Concentrations of geochemical species were compared between spring and neap tides by single factor analysis of variance (ANOVA).

Pressure head data collection

In December 2005 and April 2006, monitoring wells 2, 5, and 6 (Fig. 1) were instrumented with pressure

data loggers (Onset© HOBO Water Level Logger, model U20-001-001) that remained submerged for 2 months of data collection. In addition, well 5 was instrumented with a second pressure logger suspended in the well housing above the water level to correct for changes in barometric pressure. All pressure data was corrected to a common depth and data from wells 2 and 5 were used to constrain the pressure gradient across the model domain.

Radium sampling

GW samples were collected in August 2004 for the determination of the activities of ^{228}Ra and ^{226}Ra. After geochemical sampling (described above), multiple GW samples (5 l each) were collected over a 4-day period. The GW sample was passed through a column of MnO_2-coated acrylic fiber at a rate of <1 l min^{-1} to quantitatively collect radium (Moore 1976). The fiber was collected in a plastic bag and the long-lived radium isotope activities were determined using a gamma ray spectrometer (Moore 1984). Approximately 20 l samples were collected from the Duplin River and processed in the same manner.

Ammonium adsorption

Ammonium adsorption coefficients were determined for sediments within the saturated zone of the MH upland at 2 m depth within 1.5 m of well 5. Incubations were carried out at five salinities ranging from 1 to 28. Incubations were performed in duplicate on 1.2 g of wet sediment in 15 ml centrifuge tubes amended with 10 ml of artificial seawater at the appropriate salinity and a final NH_4^+ concentration of 100, 500, or 1000 μmol NH_4^+ l^{-1}. Concentrations of dissolved NH_4^+ were quantified in the supernatant after a 24 h incubation, and the exchangeable NH_4^+ was determined by adding 10 ml of 2 N KCl to the sediment after the supernatant had been collected (Seitzinger et al. 1991; Morse and Morin 2005).

Modeling methods

The well transect was represented by a 60 m × 4.5 m saturated model domain (dashed line in Fig. 1, encompassing wells 2–5 and containing the entire salt-freshwater transition). The distribution of 23 chemical species was computed for spring and neap tide conditions. The concentrations of biogeochemical constituents were calculated subject to advective and diffusive/dispersive transport and reactions:

$$\frac{\partial \xi C_i}{\partial t} = \nabla \cdot (D^* \nabla C_i - \mathbf{u} C_i) + \xi R_i \quad (1)$$

where ξ is porosity for solutes and 1 − porosity for solids, D^* is the dispersion tensor, C_i is concentration of species i, R_i the corresponding net reaction rate and $\mathbf{u}$ the Darcy velocity. A detailed description of the governing equations is given in Appendix 1. In brief, the temporal evolution of the concentration fields is calculated by first determining $\mathbf{u}$ from the computed pressure distribution taking into account density variations as a function of salinity. Then Eq. 1 is solved using a finite element approximation. Porosity was set to the average value measured in multiple upland cores for depths within the model domain, and the intrinsic permeability—used to relate the measured pressure heads to computed flow velocities—was set to the average of all hydraulic conductivities reported for MH (Schultz and Ruppel 2002). The dispersion coefficient was parameterized following Scheidegger (1961), with the longitudinal dispersivity for the 60 m long model domain set to an average value for sandy sediments ($\alpha_L = 0.3$ m; Moltyaner et al. 1993) and the transverse dispersivity (α_T) set to 10% of the longitudinal dispersivity. For solids, the transport terms were set to 0. All model parameters, including those for the reactions (see below) are assumed spatially constant, and do not reflect potential but unknown variations in subsurface characteristics. For a complete list of both transport and reaction parameters see Appendix 3.

At the upland model boundary, located between wells 1 and 2, concentrations and pressure were imposed based on field measurements in these two wells averaged over multiple sampling dates (Table 1). Top and bottom boundaries of the model domain are closed, reflecting the low direct impact of rain over long time periods ($\sim$130 cm year^{-1}; SINERR/GCE/UGAMI weather station at Marsh Landing, Sapelo Island, Georgia). On the saltwater side, pressure was imposed based on the field data, and chemical constituents were subject to either in- or outflow. Outflowing solute fluxes were derived from computed concentrations inside the model domain, while the composition of the inflowing water

Table 1 Boundary conditions (mol m^{-3}, except for pH)

Species	Upland boundary	Marsh-upland boundary	
	Spring and neap	Spring	Neap
Salt	1	25	25.33
[DOM]	0.207	0.401	0.599
[O_2]	0.019	0.016	0.006
[DIC]	4.72	4.52	6.56
[NO_3^-]	0.001	0.021	0.007
[NH_4^+]$_{DISS}$	0.003	0.008	0.032
[Mn^{2+}]	0	0	0
[Fe^{2+}]	0.001	0.004	0.004
[SO_4^{2-}]	0.82	19.94	18.72
[TS]	0	0	0
[CH_4]	0	0	0
[Ca^{2+}]	0	0	0
[MnO_2]	0	0	0
[$Fe(OH)_3$](s)	0	0	0
[$MnCO_3$](s)	0	0	0
[$FeCO_3$](s)	0	0	0
[FeS](s)	0	0	0
[$CaCO_3$](s)	0	0	0
[$CaSO_4$](s)	0	0	0
[S^0](s)	0	0	0
[NH_4^+]$_{ADS}$(s)	0.045	0	0
[ALK]	3.584	3.985	5.116
pH	6.85	7.22	6.9

Upland refers to the concentrations set at the right hand upstream boundary. These values are fixed and set to average concentrations determined from well 1 and 2. Salinity is set to 1 to reflect the fresh endmember composition, and the sulfate concentration was lowered to 0.82 mM assuming the composition of diluted seawater

Spring and *neap* at the *marsh-upland boundary* refer to inflowing concentrations for spring and neap tides, respectively, determined from measurements in the Duplin and well 6 (see "Methods" for details). It was assumed that the O_2 from the Duplin water was used up by nitrification, and the nitrate and ammonium concentrations derived from the salt mixing calculations were adjusted accordingly

Concentrations are in moles m^{-3}_{fluid} for solutes and moles m^{-3}_{solid} for solids. Alkalinity is calculated from the measured pH, DIC, and TS concentrations

(Table 1) was a mixture of Duplin water and well 6, whose screened depth captures the signature of deep marsh pore water. The relative contribution of these two water bodies was determined based on measured salinities, so that they match the salinity for well 5, located next to the domain boundary. The contribution of water from well 6 varied between spring (35%) and neap (78%) tides, with the remaining water attributed to the Duplin. To assess the dominant causes for the observed spring-neap variation in the MH subsurface biogeochemistry, model simulations were run to steady state for the spring and neap tide endmember settings (Table 1).

Reaction network

Net reaction rates (Eq. 1) were computed based on individual process rates and reaction stoichiometries. The reaction network encompasses primary reactions involving the oxidation of organic matter, secondary reactions involving the re-oxidation of reduced metabolites, mineral precipitation and dissolution, sorption–desorption and acid–base equilibria (Appendix 2), and was parameterized using literature and empirical data (Appendix 3). The degradation of organic matter was assumed to be first order with respect to the available reactive organic matter, which was assumed to be predominantly dissolved and whose composition was approximated by Redfield stoichiometry. The contribution of different pathways to the total rate of organic matter degradation ("primary reactions") was implemented using Monod expressions (Eq. 2). If the concentration of the oxidant for any given primary reaction is sufficiently high the reaction proceeds essentially unhindered; however, at low concentrations of the electron acceptor, its availability becomes limiting, allowing other metabolic pathways to occur. The breakdown of organic matter was formulated as a progression of primary reactions, from aerobic respiration, to dissimilatory nitrate reduction, manganese oxide reduction, iron oxyhydroxide reduction, sulfate reduction and methanogenesis, reflecting differences in energy yield (e.g., Froelich et al. 1979; Hunter et al. 1998; Appendix 2):

$$\mathrm{pr}_j = \left(k_{\mathrm{DOM}} \cdot [\mathrm{DOM}] - \sum_{n=1}^{j-1} \mathrm{pr}_n \right) \cdot \frac{[C]_j}{[C]_j + Km_j} \qquad (2)$$

where pr_j refers to the rate for primary reaction j, k_{DOM} is the first order rate constant, [DOM] is the reactive dissolved organic matter concentration, Km and $[C]$ are the half saturation constant and the concentration of the respective terminal electron

acceptor (O_2, NO_3^-, MnO_2, $Fe(OH)_3$, and SO_4^{2-}) in reaction j, respectively.

Special consideration was given to the partitioning of NO_3^- between the two dissimilatory nitrate reduction pathways implemented in the model, as the resulting N-products differ in their bioavailability, with N_2 production reflecting net nitrogen loss from the system. The relative importance of DNF and DNRA has been linked to two factors that were deemed pertinent in this system: (1) the concentration of sulfide ($TS = H_2S + HS^- + S^{2-}$) and (2) the ratio of available electron donor to electron acceptor. At relatively low TS concentrations (<20 μmol l^{-1}) a strong inhibitory effect on DNF—but not DNRA—was observed in laboratory incubations of Satilla River (GA) intertidal sediment (Porubsky et al. 2009). Inhibition of DNF by TS was expressed via the fraction of the DNF rate that occurs at a given sulfide concentration:

$$f_S = \left(\max\left(TS_{DNF}^{MIN}, [TS]\right)/TS_{DNF}^{MIN}\right)^{-0.675} \quad (3)$$

where TS_{DNF}^{MIN} is a minimum concentration of 1.5 μmol TS l^{-1} that causes inhibition.

The availability of electron donor relative to electron acceptor, reflected by the DOM/NO_3^- ratio, has been proposed to control the balance of DNF and DNRA (Tiedje et al. 1982). Based on experimental data from intertidal sediments (Porubsky et al. 2009), a linear relationship between the DOM/NO_3^- and the DNRA/DNF was applied, with higher DOM/NO_3^- ratios correlating with increased DNRA activity relative to DNF:

$$(DNRA/DNF) = 0.0629 \cdot \left(DOM/NO_3^-\right) - 0.4481 \quad (4)$$

where DNRA/DNF, constrained to a minimum value of 1%, represents the ratio of the rates of DNRA and DNF, so that the ratio of DNF to the total nitrate reduction rate (f_R) can be expressed as:

$$\begin{aligned} f_R &= (DNF/(DNF + DNRA)) \\ &= (1 + (DNRA/DNF))^{-1} \end{aligned} \quad (5)$$

Combined, the ratio of DNRA/DNF and the inhibition of DNF by sulfide yield the fraction of the total NO_3^- reduction rate available to DNF ($pr_{2,DNF}$) and DNRA ($pr_{2,DNRA}$), respectively:

$$pr_{2,DNF} = pr_2 \cdot f_S f_R \quad (6)$$

$$pr_{2,DNRA} = pr_2 - pr_{2,DNF} = pr_2(1 - f_S f_R) \quad (7)$$

Primary reactions lead to the production of reduced inorganic species that can then be re-oxidized by chemical or microbially-mediated reactions (Appendix 2). These secondary reactions were described by bimolecular rate laws (Hunter et al. 1998):

$$sr_j = sk_j \cdot [RED] \cdot [OX] \quad (8)$$

where sr_j is the jth secondary reaction rate, sk_j is the jth apparent rate constant, and [RED] and [OX] represent the concentration of the reductant and the oxidant, respectively. In addition, sulfide inhibition of nitrification (sr_4; Appendix 2) was taken into account through an inhibition factor (f_{NITR}), which was used as a multiplier in Eq. 8 (obtained from fitting the data in Joye and Hollibaugh 1995):

$$f_{NITR} = \max\left(0,\ 1 - 5.8 \cdot [TS] - 41.7 \cdot [TS]^2\right) \quad (9)$$

where TS is in mmol l^{-1}.

Mineral precipitation–dissolution reactions (Appendix 2) were considered reversible and dependent on the saturation state Ω_j of each mineral, which was determined from the activities of the species involved in the reaction and the equilibrium constant (Appendix 3). The general forms of the precipitation and dissolution reactions, respectively, are:

$$\begin{aligned} mr_j^{PREC} &= mk_j^{PREC} \cdot \left(\Omega_j - 1\right) \quad \text{for } \Omega_j \geq 1 \\ mr_j^{DISS} &= mk_j^{DISS} \cdot \left[C_j\right] \cdot \left(1 - \Omega_j\right) \quad \text{for } \Omega_j < 1 \end{aligned} \quad (10)$$

where mr_j^{PREC} and mr_j^{DISS} are the precipitation and dissolution rates for the jth mineral, mk_j^{PREC} and mk_j^{DISS} are the corresponding apparent rate constants, and $[C]_j$ is the concentration of mineral j.

In contrast to the above kinetic description of reactions, concentrations of chemical species subject to rapid acid–base reactions were determined from the modeled DIC and TS assuming local equilibrium, taking into account the ionic strength (derived from salinity) and the groundwater pH. The latter was obtained by identifying the pH at which the modeled alkalinity ($= 2CO_3^{2-} + HCO_3^- + OH^- + 2S^{2-} + HS^- - H^+$) was consistent with DIC and TS concentrations. In an iterative approach (Luff et al. 2001), at each computational node and timestep, activity coefficients were expressed as a function of ionic strength and [H^+] was computed using a

Newton–Raphson root finding algorithm (Press et al. 1992).

Reflecting the rapid and reversible exchange between dissolved and adsorbed NH_4^+ (Rosenfeld 1979), ammonium sorption was also part of the equilibration module in which total ammonium was distributed between the sorbed and dissolved phase, using the experimentally determined value of the apparent adsorption coefficient K_n as a function of salinity (Appendix 2; see below).

Results

Field and laboratory data

Groundwater biogeochemistry

The well transect at MH was sampled at low tide during four spring tides and five neap tides (Table 2; Fig. 2). Only small differences in the median salinity values for each well (Fig. 2a) were observed between spring versus neap tides; the highest salinities were observed near the saltmarsh-upland boundary and salinity decreased toward the upland. The range of salinity was greatest in well 2 and to a lesser extent well 3, which are located in the saltwater/freshwater transition zone (Figs. 2a, 6). pH values were typically below 7 and showed little variation across spring-neap tides or seasons (Table 2). Oxygen concentrations were typically below 20 μmol l^{-1} and O_2 concentrations in the adjacent Duplin River were ~250 μmol l^{-1} (Table 2). Dissolved inorganic carbon concentrations were on the order of 1–10 mmol l^{-1} and showed considerable variation among the wells with no clear spring-neap or seasonal patterns (Table 2).

DOC concentrations were lowest in well 1, the most upland well (Table 2; Fig. 2b). Higher DOC concentrations were observed in the other wells, and concentrations were generally higher and more variable during neap tide (Fig. 2b). However, even the substantially higher median DOC concentrations in wells 5 and 6 did not exhibit a significant difference between spring and neap tide ($p > 0.5$ for well 5 and $p > 0.2$ for well 6, Fig. 2b). Concentrations of DOC in the Duplin were similar to those in wells 5 and 6 during spring tides (Fig. 2b).

Median concentrations of oxidized nitrogen species (NO_x) were below 10 μmol l^{-1} in all wells during neap tides (Table 2; Fig. 2c). During spring tides, however, the two wells closest to the Duplin (5 and 6) exhibited median concentrations of approximately 20 μmol NO_x l^{-1}. Spring tide NO_x concentrations in well 5 were significantly higher than neap tide concentrations ($p < 0.05$). NO_x concentrations in well 1, the furthest upland, were approximately 1 μmol l^{-1} during both spring and neap tides and below that in the Duplin (Fig. 2c).

The median NH_4^+ concentration in well 1 was approximately 2 μmol l^{-1} during both spring and neap tides (Table 2; Fig. 2d). During spring tides, NH_4^+ concentrations were ≤10 μmol l^{-1} in wells 4–6 (Fig. 2d). Ammonium concentrations reached approximately 20 μmol l^{-1} in wells 2 and 3 for both spring and neap tides. Wells 4, 5 and 6 had significantly ($p < 0.05$) higher NH_4^+ concentrations (by four times) during neap tides compared to spring tides (Fig. 2d).

Iron concentrations were low in the upland and the marsh, and showed a maximum in well 3 for both spring and neap tides. Sulfate concentrations were low in the upland (well 1) and increased in well 2 but showed little variation in the other wells. Total sulfide concentrations were between 0 and 4 μmol l^{-1} throughout the well transect (Table 2).

Groundwater transport

Data retrieved from the pressure loggers showed larger diurnal pressure fluctuations during spring tides compared to neap tides but a rather constant diurnally averaged pressure gradient. Diurnal variations in pressure were highest in well 6 and decreased toward the upland as the tidal influence was attenuated. Precipitation events were evident in the observed freshwater heads, but this had little effect on the pressure gradient across the domain (Fig. 3a, b).

The Duplin River was significantly enriched in ^{226}Ra and ^{228}Ra relative to surface seawater and exhibited a high $^{228}Ra/^{226}Ra$ activity ratio. The $^{228}Ra/^{226}Ra$ activity ratio of well 5 qualitatively matches that measured in the Duplin (Fig. 4). Well 6, which was closest to the Duplin, had a lower $^{228}Ra/^{226}Ra$ activity ratio and higher ^{226}Ra concentration than the Duplin or wells 4 and 5. Well 1 did

Table 2 Groundwater biogeochemical field data

Date	Well	Salinity	pH	O_2	DIC	DOC	NO_x	NH_4^+	Fe^{2+}	SO_4^{2-}	TS
Neap tide											
Apr 2003	1	1	–	–	7300.0	148.6	0.4	0.0	3.1	0.3	–
Aug 2003	1	1	–	–	–	154.2	2.5	0.9	0.2	0.1	–
Apr 2004	1	3	6.6	28.1	4000.0	280.1	1.0	7.3	1.4	0.1	0.0
Jun 2004	1	3	7.0	14.4	–	269.5	1.0	1.6	1.2	0.1	0.0
Dec 2004	1	–	–	–	3950.0	285.3	–	–	–	–	0.3
Apr 2003	2	9	–	–	4380.0	172.7	4.0	26.7	1.5	2.4	–
Aug 2003	2	6	–	–	–	228.6	0.4	28.4	16.2	3.2	–
Apr 2004	2	20	6.3	6.9	2720.0	1038.2	0.8	36.3	5.4	13.0	2.3
Jun 2004	2	19	6.5	9.4	–	1113.2	1.0	38.3	3.3	11.8	0.0
Dec 2004	2	–	–	–	2600.0	858.1	–	–	–	–	1.2
Apr 2003	3	28	–	–	4960.0	979.5	0.3	33.8	88.7	20.7	–
Aug 2003	3	23	–	–	–	809.4	0.3	25.2	61.3	16.0	–
Apr 2004	3	27	6.4	4.7	2490.0	801.5	0.3	33.2	85.5	19.9	0.3
Jun 2004	3	27	6.3	8.4	–	922.9	0.7	15.1	42.5	19.4	0.0
Dec 2004	3	–	–	–	2810.0	765.4	–	9.7	–	–	3.6
Apr 2003	4	–	–	–	–	–	–	–	–	–	–
Aug 2003	4	27	–	–	–	908.5	1.7	20.8	15.2	19.6	–
Apr 2004	4	25	6.4	7.8	2130.0	367.2	12.9	31.7	15.3	19.5	0.2
Jun 2004	4	25	6.5	14.7	–	494.5	6.6	19.8	4.8	17.6	0.0
Dec 2004	4	–	–	–	2340.0	472.2	–	–	–	–	1.0
Apr 2003	5	28	–	–	4250.0	255.7	–	–	0.3	21.8	–
Aug 2003	5	25	–	–	–	834.4	8.2	43.5	4.7	18.2	–
Apr 2004	5	23	6.5	10.6	2320.0	343.0	2.0	48.5	7.3	17.8	0.2
Jun 2004	5	–	–	–	1690.0	–	–	–	–	–	0.0
Dec 2004	5	–	–	–	–	940.6	–	–	–	–	0.4
Apr 2003	6	25	–	–	10240.0	401.8	0.3	53.8	1.5	18.9	–
Aug 2003	6	22	–	–	–	763.0	3.4	21.9	48.9	16.0	–
Apr 2004	6	24	6.6	–	3150.0	438.6	5.9	34.8	23.6	18.2	1.3
Jun 2004	6	25	6.6	8.1	–	936.7	0.4	46.4	–	17.5	0.4
Dec 2004	6	–	–	–	3240.0	856.1	–	–	–	–	0.6
Apr 2003	Duplin	–	–	–	–	–	–	–	–	–	–
Aug 2003	Duplin	–	–	–	–	–	–	–	–	–	–
Apr 2004	Duplin	28	6.6	231.9	1930.0	116.6	0.4	2.3	1.4	21.5	0.1
Jun 2004	Duplin	32	6.8	–	–	523.1	0.4	0.2	0.7	23.6	0.0
Dec 2004	Duplin	–	–	–	2100.0	–	–	2.3	–	–	0.6
Spring tide											
Apr 2002	1	0	–	–	9207.4	104.9	1.1	1.2	–	0.1	–
Aug 2003	1	0	–	–	–	128.8	1.8	1.5	0.2	0.1	–
Jan 2004	1	0	6.9	15.0	3732.4	287.3	1.2	9.4	0.7	0.1	0.0
Jun 2004	1	1	6.9	18.1	140.0	–	–	–	0.8	–	0.3
Apr 2002	2	8	–	–	7283.2	658.7	15.3	9.3	–	9.0	–
Aug 2003	2	2	–	–	–	175.4	0.4	25.3	23.4	1.8	–
Jan 2004	2	20	6.2	4.7	1968.7	921.9	0.4	39.1	5.4	12.0	0.0
Jun 2004	2	19	6.0	7.5	–	–	–	–	2.2	–	0.7

Table 2 continued

Date	Well	Salinity	pH	O_2	DIC	DOC	NO_x	NH_4^+	Fe^{2+}	SO_4^{2-}	TS
Apr 2002	3	25	–	–	6880.6	779.1	0.2	18.7	–	20.2	–
Aug 2003	3	14	–	–	–	1090.4	13.6	17.6	39.9	11.7	–
Jan 2004	3	29	6.5	4.7	2035.4	814.0	0.1	24.0	87.2	20.6	0.0
Jun 2004	3	27	6.4	6.6	–	–	–	–	0.3	–	3.9
Apr 2002	4	26	–	–	5120.5	252.1	14.2	11.8	–	21.5	–
Aug 2003	4	25	–	–	–	745.1	0.3	4.2	13.8	19.9	–
Jan 2004	4	25	6.7	7.8	1987.5	420.3	6.2	6.5	16.7	18.1	0.0
Jun 2004	4	24	6.4	5.0	–	–	–	–	1.6	–	0.9
Apr 2002	5	25	–	–	–	–	–	–	–	–	–
Aug 2003	5	25	–	–	–	398.8	17.3	2.0	3.5	19.5	–
Jan 2004	5	–	6.7	15.6	–	410.0	21.1	12.8	4.0	18.3	0.0
Jun 2004	5	–	–	–	1855.3	–	–	–	–	–	–
Apr 2002	6	21	–	–	7860.2	316.4	3.6	11.1	–	16.4	–
Aug 2003	6	20	–	–	–	468.9	18.3	12.8	0.4	16.0	–
Jan 2004	6	24	6.9	–	–	623.8	45.4	–	–	17.1	2.3
Jun 2004	6	24	–	–	–	–	–	–	–	–	1.7
Apr 2002	Duplin	26	–	–	4504.3	398.7	0.7	4.0	–	20.4	–
Aug 2003	Duplin	26	–	–	–	336.0	0.7	0.5	–	–	–
Jan 2004	Duplin	29	7.2	267.2	1560.6	481.2	0.3	1.7	0.1	21.4	0.0
Jun 2004	Duplin	–	7.5	251.3	2008.0	–	–	–	6.6	23.7	0.2

Concentrations are in μmol l^{-1}, except for SO_4^{2-} which is in mmol l^{-1}

not experience elevated salinity levels, thus rates of Ra desorption were low as reflected in the low Ra concentrations (Fig. 4).

Ammonium adsorption

Ammonium adsorption coefficients (K_n, defined as the equilibrium ratio of sorbed to dissolved ammonium concentrations) were determined for MH upland soil at a depth of approximately 2 m, within 1.5 m of well 5 (Fig. 5). A decrease of K_n resulted from increased salinity; a K_n value of approximately 1.4 was observed at a salinity of 28 while the K_n was 3.5 at a salinity of 1.

Modeling results

Flow and salinity patterns

The pressure loggers indicated no significant difference in the tidally averaged pressure gradient between spring and neap tides (Fig. 3b). Using the pressure field measurements to impose a freshwater head across the domain (Appendix 3) led to modeled saline water intruding approximately 50 m into the upland (Fig. 6). The steady state simulation results match the salinity values determined in the field, with wells 2 and 3 being located in the fresh-saltwater transition zone (Figs. 2a, 6).

Organic matter reactivity

The mixing of two water bodies of distinct redox chemistry and the breakdown of DOM are the main drivers for biogeochemical reactions in groundwater. Both factors differed between neap tide and spring tide, with the inflowing spring tide water lower in DOM and NH_4^+ but higher in O_2 and NO_3^- (Table 1).

Because total DOM measurements may provide a poor approximation of the reactive substrate concentrations, and due to the large range of DOM degradation rates reported in the literature (Hunter et al. 1998 and references therein), the DIC

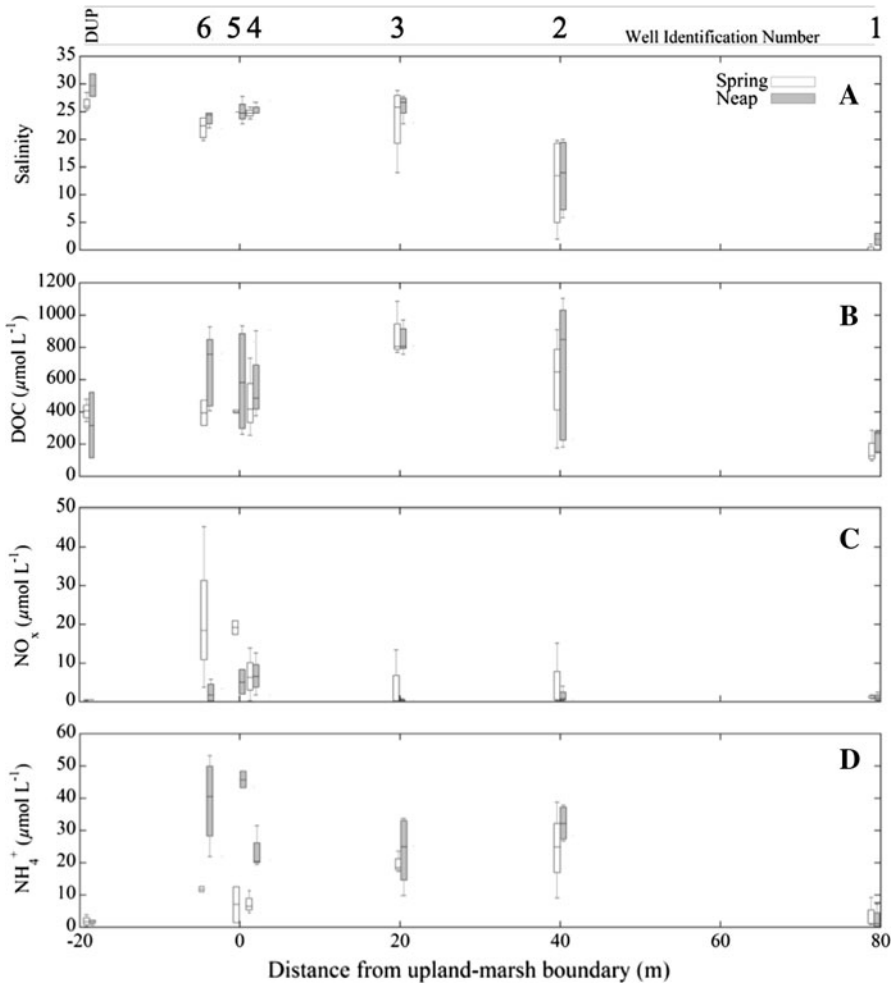

Fig. 2 Boxplot of groundwater data for spring tides (*white bars*) and neap tides (*dark bars*). Wells are identified in the top panel, and boxes appear relative to the spatial distribution of the wells (*x*-axis). DUP denotes the Duplin River. **a** Salinity, **b** DOC, **c** NO_x and **d** NH_4^+ data for the MH well transect. *Boxplots* illustrate the lowest non-outlier observation, the lower quartile, the median, the upper quartile, and the highest non-outlier observation

concentrations measured in the field were used to constrain the DOM degradation rate, $R = k_{DOM} \cdot [DOM]$. The value of k_{DOM} was set to $\sim 3 \times 10^{-4}$ year^{-1} (Appendix 3), resulting in an increase in DIC from the upland to the marsh that was comparable to the observations.

Nitrogen cycling

Modeled NO_3^- values reached a maximum of approximately 25 μmol NO_3^- l^{-1} at the saltmarsh-upland boundary (Fig. 7a) in spring tide simulations. Nitrate concentrations of approximately 5 μmol l^{-1} persist to approximately 6.5 m into the domain. Nitrate concentrations in the neap tide simulation matched the values measured in the field (Figs. 2c, 7b), and were much lower than in the spring tide simulation.

Simulated dissolved ammonium ($NH_4^+{}_{DISS}$) concentrations were approximately 10 μmol l^{-1} within 10 m of the saltmarsh-upland boundary (Fig. 7c) and increased to approximately 40 μmol l^{-1} at 20 m under spring tide conditions. Dissolved NH_4^+ concentrations in neap tide simulations were approximately 3.5 times higher than the corresponding spring tide values (Fig. 7c, d). Modeled $NH_4^+{}_{DISS}$ concentrations between 10 and 20 m showed a similar pattern for both spring and neap tide simulations and were slightly higher than the concentrations determined in the field (Figs. 2d, 7c, d).

Adsorbed ammonium ($NH_4^+{}_{ADS}$) presented a similar pattern as $NH_4^+{}_{DISS}$ at the saltmarsh-upland boundary, where the modeled $NH_4^+{}_{ADS}$ concentration was approximately 20 μmol dm^{-3}_{solid} (Fig. 7e) under spring tide conditions. Further into the domain where salinity was lower, the ratio of $NH_4^+{}_{ADS}$ to

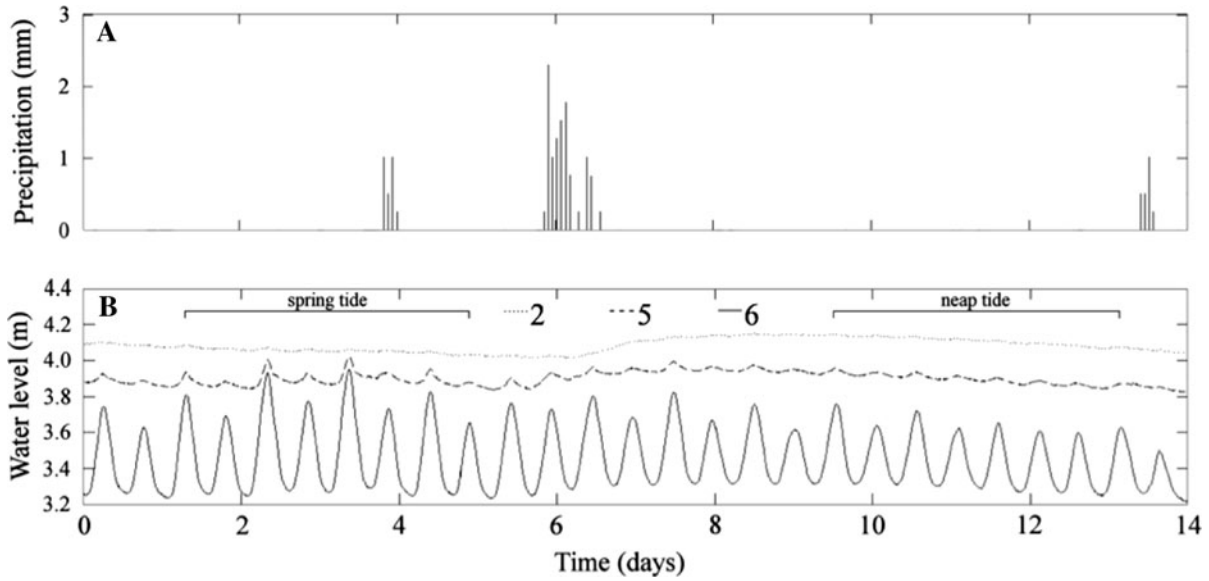

Fig. 3 Precipitation data (**a**) from the SINERR/GCE/UGAMI weather station at Marsh Landing, Sapelo Island, Georgia from December 12–24, 2005, and corresponding well water levels (**b**) corrected to a common depth

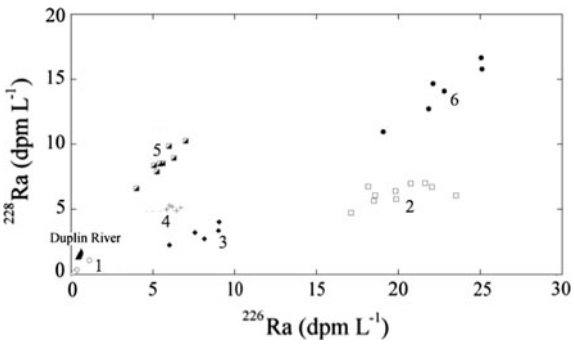

Fig. 4 Radium data collected from the MH well transect in August 2004. Like *symbols* are replicates from the same well collected at different tide stages over 5 days. *Labels* identify each well and the Duplin River

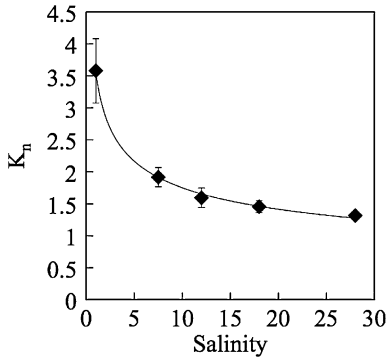

Fig. 5 Measured ammonium adsorption coefficients (K_n in $[(\text{mol/m}^3_{\text{solid}})/(\text{mol/m}^3_{\text{fluid}})] = \text{NH}^+_{4,\text{ADS}}/\text{NH}^+_{4,\text{DISS}}$) versus salinity

$NH_4^+{}_{DISS}$ increased. Adsorbed NH_4^+ concentrations were elevated at the saltmarsh-upland boundary in neap tide simulations, due to higher computed $NH_4^+{}_{DISS}$ concentrations (Fig. 7f).

Modeled peak nitrification rates were highest (6.9 μmol N m^{-3} h^{-1}) in the spring simulation and were confined within 1 m of the saltmarsh-upland boundary. Nitrification rates declined rapidly with increasing distance from the marsh and were O_2 limited (inferred from modeled O_2 concentrations, data not shown). Nitrification showed a similar distribution in the neap tide simulation with peak rates approximately 25% lower than rates during spring tide. Modeled peak DNF rates in the spring tide simulation were also highest near the saltmarsh-upland boundary (0.6 μmol N m^{-3} h^{-1}) where NO_3^- concentrations were highest (Fig. 7a). Rates quickly decreased with distance into the upland and were limited by NO_3^- availability. Peak DNF rates were 3 times lower in the neap tide simulation than in the spring tide simulation. Lower DNF rates in the neap tide simulation correlated with both lower NO_3^- concentrations (Fig. 7b) and higher DOM concentrations (not shown). The resulting higher DOM/NO_3^-

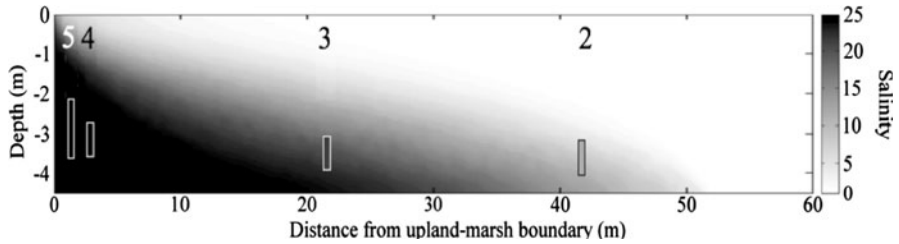

Fig. 6 Modeled and field measured salt distributions. Small *inset boxes* represent the screened interval for each well, with the grayscale illustrating the median measured (spring tide) salinities for each well

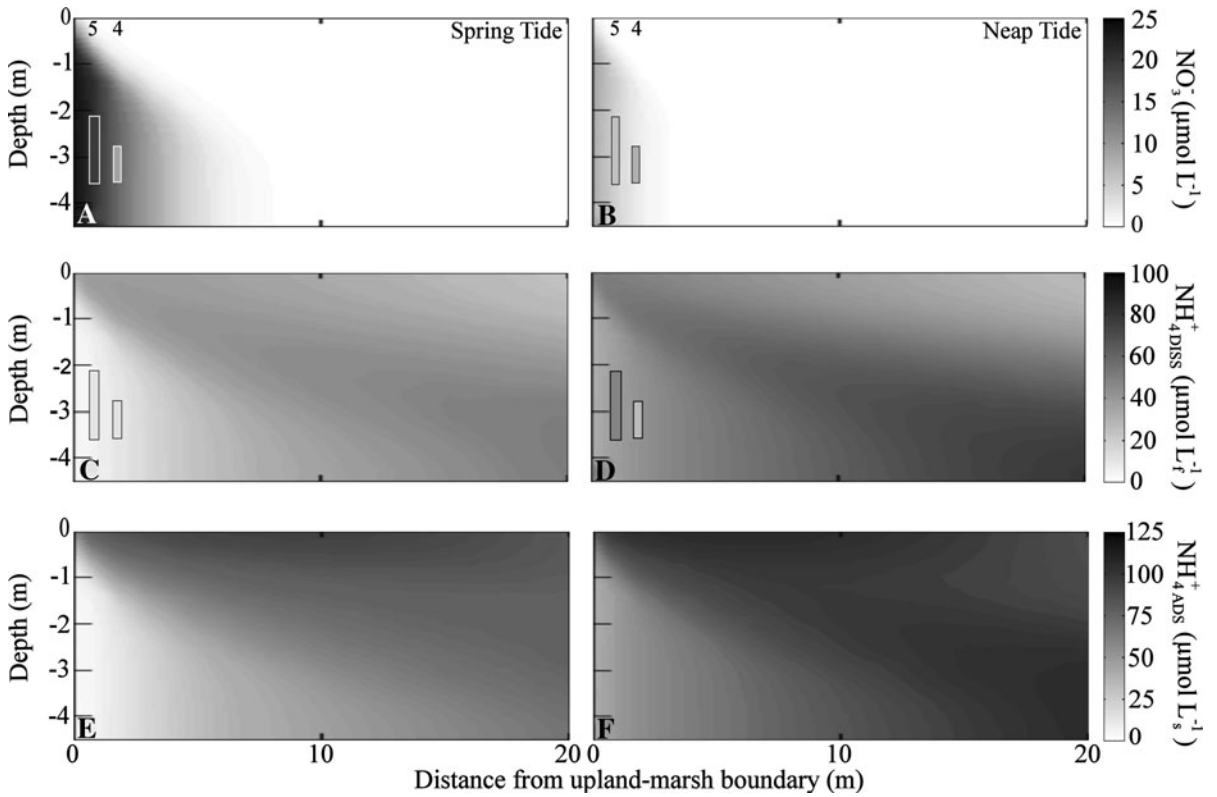

Fig. 7 Modeled nitrogen species distributions. Each panel illustrates the first 20 m of the domain for either the spring tide (*left panels*) or neap tide (*right panels*) simulations. **a**, **b** Depict the modeled NO_3^- distribution; **c**, **d** depict the modeled $NH_4^+{}_{DISS}$ distribution; and **f**, **g** depict the modeled $NH_4^+{}_{ADS}$ distribution. Small *inset boxes* (**a**–**d**) represent the screened interval for the depicted well, with the *grayscale* illustrating the median measured concentrations for each well

ratio favored DNRA, which exhibited its peak rates (0.6 µmol N m^{-3} h^{-1}) near the saltmarsh-upland boundary under neap tide conditions. As with DNF, the modeled maximum DNRA rate corresponded to zones with the highest NO_3^- values. Under neap tide conditions simulated peak DNRA rates were approximately three times higher than the peak DNF rates found in the domain, while at spring tide, the model estimated peak DNRA rates were approximately 30% lower than the maximum DNF rates.

Discussion

Interpretation of model results allows for a parsimonious assessment of the role of microbial N transformations, sorption processes and transport dynamics. The complexity of the natural environment and missing constraints—e.g., on organic matter composition and its variability, on subsurface heterogeneity, or related to limited spatial resolution of the available data—introduce uncertainty and pose formidable

challenges in such an analysis. However, despite these potential shortcomings, integration of field data with mechanistic modeling, augmented with data from laboratory experiments, helps constrain the dominant processes taking place in the groundwater at the fresh-saltwater transition zone.

Microbial processes

The concentration and speciation of DIN can be altered by a number of microbially mediated processes including nitrification, denitrification, DNRA, and anammox. While the anammox process is potentially capable of removing N from the subsurface, it occurs at only low rates in nearby coastal marsh sediments ($\sim$6% of the total N_2 production; Porubsky et al. 2009). So, this process was not considered in the current model.

Nitrification could potentially impact the redox switch observed in well 5 by oxidizing the larger neap tide NH_4^+ pool around this well. However, simulations indicate that nitrification was of minor importance within the model domain. While modeled peak nitrification rates are on the low end of nitrification rates reported in the literature (Böhlke et al. 2004; Vervaet et al. 2004; Smith et al. 2006) simple mass balance considerations support this general finding. If all O_2 in the 0–10 m zone near well 5 was used to fuel nitrification, this would change NO_3^- by <1%. Similarly, with low O_2 concentrations in the inflowing water, compared to NO_3^- during both spring and neap tides, complete use of the inflowing O_2 by nitrification would maximally increase the NO_3^- flux by $\sim$40%, which is insufficient to explain the observed NO_x concentration variation in well 5. Therefore, while nitrification was occurring in the domain, O_2 limitation restricts its importance in the upland aquifer.

Since DNF and DNRA impact concentration, speciation and bioavailability of the DIN pool in different ways, it is important to understand the factors regulating the balance of the two processes. Potential factors that can control the balance of DNF and DNRA include temperature (Kelly-Gerreyn et al. 2001), O_2 content (Fazzolari et al. 1998; Silver et al. 2001), sulfide concentration (An and Gardner 2002), and the DOM/NO_3^- ratio (Tiedje et al. 1982; Porubsky et al. 2009). Neither temperature nor O_2 are likely causes for any potential switch between the DNF and DNRA at MH due to the small range of temperatures encountered over a spring-neap tidal cycle (average 1°C difference in well 5 between spring and neap tides, with an approximately 3°C seasonal range) and the limited change in the O_2 content (5–15 μmol l^{-1}) observed over both spring-neap tidal cycles and throughout the year. Similarly, measured sulfide concentrations in the wells near the upland-marsh boundary were typically zero, and model simulations do not indicate significant sulfide levels near the upland-marsh boundary, so sulfide could not be responsible for a switch between DNF and DNRA. Sulfide inhibition of both DNF and nitrification at TS $\leq$20 μmol l^{-1} (Gould and McCready 1982; Jensen and Cox 1992; Joye and Hollibaugh 1995) are unlikely to impact the balance of the two processes in the area surrounding well 5. However, differences in the DOM content of the inflowing saline water during spring tide (0.4 mmol C l^{-1}) and neap tide (0.6 mmol C l^{-1}) alters the DOM/NO_3^- ratio in the area around well 5 (Table 1). The changes in DOM concentration shift the balance of DNF and DNRA toward DNRA under neap tide conditions (Eq. 4), which promotes higher NH_4^+ concentrations in the area around well 5 (Fig. 7d).

To assess whether the differences in modeled DNF and DNRA rates were large enough to cause the observed switch in the composition of DIN between spring and neap tides, the computed rates of DNF and DNRA were integrated over the 10 m nearest the marsh-upland boundary over which variations in DIN pools were observed (Fig. 7) for both spring tide and neap tide endmember conditions. Under spring tide conditions, $\sim$34 μmol NO_3^- day^{-1} was reduced by DNF, about ten times more than under neap tide conditions. However, DNRA rates exceeded DNF rates by a factor of 2–11 for spring and neap tides, respectively. A higher rate of DNRA under spring tide conditions ($\sim$56 μmol N day^{-1}) than under neap tide conditions ($\sim$35 μmol N day^{-1}) contradicts the observed lower NH_4^+ concentrations in well 5 at spring tide and thus is not capable of causing the observed redox switch.

Higher NH_4^+ concentrations under neap conditions could result from increased NH_4^+ production via organic matter degradation of a larger DOM pool. However, the integrated net rate of NH_4^+ production,

resulting from production by the degradation of DOM via primary reactions, DNRA, and losses from nitrification, was similar under spring and neap tide conditions ($\sim 86 \pm 21$ μmol N day^{-1}). Although the model simulations showed DNF rates which starkly differed between spring and neap tides, these denitrification rates were much lower than the computed DNRA rates and total NH_4^+ production rates, both of which showed much lower spring-neap variation (22–42%) than DNF. The lack of variability in net NH_4^+ production between spring and neap tide conditions can therefore not account for the observed change in NH_4^+ concentration in well 5.

Ion exchange processes

Laboratory assays showed a strong dependency of ammonium sorption on pore water salinity, such that as the salinity increases, NH_4^+ desorbs (Fig. 5; Seitzinger et al. 1991). The sorbed pool is particularly sensitive to changes in salinity at the fresh endmember, e.g., associated with an inland migration of the saltwater wedge. In the field, salinity varied over a range of 5–20 in well 2. To assess the potential impact that such a shift would have on the dissolved and adsorbed NH_4^+ pools, we compared the sorbed NH_4^+ pool for two salinity distributions consistent with the observational data—one as shown in Fig. 6, the other with a saltwedge extending further inland but retaining the discharge face. After re-equilibrating the total ammonium pool, the adsorbed NH_4^+ pool in the entire domain was lower by $\sim 2\%$ in the setting with the saltwater intruding further inland. Averaged over the entire domain, the difference of 0.2 mol of NH_4^+ corresponds to an increase of ~ 1.1 μmol l^{-1} in dissolved ammonium, which exceeds the impact of microbial processes or inflow over the spring-neap tidal cycle. However, there is no indication for any significant salinity fluctuation near well 5, and the time of travel necessary for the liberated NH_4^+ at the saltwater–freshwater transition zone to reach well 5 would preclude it from impacting the NH_4^+ concentration there over a spring-neap tidal cycle. Thus, sorption–desorption mainly changes bioavailability of NH_4^+ locally, and only a prolonged change in the freshwater flow (i.e., drought conditions) could result in long term shifting of the salt wedge and lead to impacts on the DIN speciation downstream.

Transport

The two radium isotopes, ^{226}Ra and ^{228}Ra, have half-lives of 1600 and 5.7 years, respectively, and are continually produced from their long-lived parents, ^{230}Th and ^{232}Th. As a consequence of its shorter half-life, ^{228}Ra activity is replenished more quickly after removal of pore fluid (Moore 2003). The substantial Ra activities and high $^{228}Ra/^{226}Ra$ activity ratio measured in the Duplin River are consistent with a source of groundwater similar to that sampled at well 5. The radium data indicates that the area surrounding well 5 is frequently flushed and that flushing decreases inland (Fig. 4). The impact of the transport of the infiltrating water with different chemical make-ups is twofold: (1) it leads to a direct change in concentrations in the domain, and (2) it impacts the physico-chemical and microbial processes occurring within the domain.

At the marsh/upland boundary, modeled flow out of the domain is characterized by brackish water confined to the upper meter while below that flow of saline water is directed into the domain, adding both NO_3^- and NH_4^+ to the area around well 5 thus directly impacting the N speciation. The mass of NH_4^+ that enters the area around well 5 under neap tide conditions is ~ 3 times greater than the production of NH_4^+ from DNRA and approximately 1.5 times greater than the integrated net NH_4^+ production within 10 m of the marsh/upland boundary and thus dominates the pore water composition. Because of temporal variations in source water composition (Table 1) approximately three times more NO_3^- enters the domain under spring tide conditions than under neap tide, while conversely, under neap tide conditions, approximately four times more NH_4^+ is transported into the domain. Differences in NO_3^- and NH_4^+ concentrations in the saline inflowing water between spring and neap tides is the dominant factor influencing the switch between N species in the area surrounding well 5.

The factors that influence the N speciation of the marsh porewater entering the upland model domain over spring-neap tide cycles remain an area for further examination. The DIN speciation and concentrations of the Duplin River did not vary over spring/neap tidal cycles (Fig. 2c, d). Since the changes in the inflowing DIN cannot be linked to variations in the NO_3^- concentration of the Duplin, the variations must be

due to changes in the marsh porewater composition. Nitrification rates reported for surficial saltmarsh sediments (0.4–6 mmol N m^{-2} h^{-1}) are typically higher than those reported for groundwater (Anderson et al. 1997; Tobias et al. 2001; Smith et al. 2006). The increase in NO_3^- in well 6, and hence the infiltrating water at spring tide, may reflect a spring-neap tide variation in nitrification in marsh sediments, possibly the result of more oxygenated conditions. We hypothesize that at MH, decreased flushing of the upper marsh during neap tide leads to the accumulation of reduced compounds via organic matter degradation, consistent with observations elsewhere. On the York River (VA, USA; Tobias et al. 2001), variations in the NH_4^+ concentrations over spring-neap tidal cycles were driven by biogeochemical processes and flushing of the marsh, with neap NH_4^+ concentrations $\sim$3.5 times higher than spring concentrations (Vörösmarty and Loder 1994). Under spring conditions, when the upper marsh is inundated during high tides, the upper marsh is flushed with oxygenated water that stimulates nitrification, causing the low ammonium/nitrate rich water observed in well 6 that infiltrates with the inflowing saline water.

Conclusions

By using a combination of field observations, laboratory assays, and modeling, we were able to examine the biogeochemical dynamics in a coastal hammock groundwater system. Model results indicate that microbial processes impact the speciation of DIN, but the magnitude of the impact is too small to account for the observed switch in DIN speciation over spring-neap tidal cycles. Ion exchange constants determined from field samples indicated that ammonium sorption can lead to retardation of NH_4^+ transport and remove a significant fraction of NH_4^+ from the dissolved pool. While variations in pore water salinity can lead to desorption of significant amounts of NH_4^+, this process does not explain the observed switch in DIN speciation. The small variations in salt concentrations observed at well 5 near the upland-marsh boundary, together with low flow velocities prevent an efficient removal of desorbed ammonium over daily or even biweekly timescales. Instead, variations in the chemical composition of the inflowing water over spring-neap tidal cycles are predominantly responsible for the observed spring-neap redox oscillation in the upland groundwater well adjacent to the marsh. These fortnightly variations are consistently observed across all four seasons. They appear to be driven by a variation in marsh porewater composition, likely due to enhanced flushing, increased oxygenation and nitrification within the marsh. We conclude that spring-neap tidal cycles are important not only in shaping the biogeochemical environment in the marsh-upland transition zone, but likely represent a key timescale for assessing the export of nutrients to the coastal ocean.

Acknowledgments We thank C. Ruppel for installation of the well transect at Moses Hammock, and M. Erickson and N. Weston for assistance in the field and in the laboratory. This publication was supported by the Georgia Sea Grant Program of the National Sea Grant College, NOAA; under NOAA Grant NA04OAR4170033 (to CM), NA06RG0029-R/WQ11 and R/WQ12A (to SBJ) and by the NSF funded Georgia Coastal Ecosystems Long Term Ecological Research (LTER) program (OCE 99-82133 and OCE 06-20959). Comments from two anonymous reviewers improved the manuscript.

Appendix 1: Governing equations and implementation

Governing equations

The governing equation is based on conservation of fluid mass, expressed as:

$$\frac{\partial(\rho\phi)}{\partial t} = -\nabla \cdot (\rho\phi v) \tag{11}$$

where ϕ is porosity, t is time, v is fluid velocity, ∇ is the gradient operator, and ρ is fluid density, dependent on temperature (T), salinity (S) and pressure (p). Here, ρ [kg m^{-3}] is expressed as a linear function of salinity at a given temperature T*[°C]:

$$\rho(S) = 1000.0821 - 0.0324(T^* - 4) - 0.0052(T^* - 4)^2 + (0.7925 - 0.0021(T^* - 4))S \tag{12}$$

which is based on a polynomial fit to the UNESCO equation of state ρ (S,T,p), with an error <0.3 kg m^{-3} for $0 < S < 35$, $4 < T < 35$°C at $p = 1$ bar. Assuming constant temperature and porosity, the left hand side of Eq. 11 is approximated by $\gamma\phi\frac{\partial S}{\partial t} + \beta\phi\frac{\partial p}{\partial t}$,

where the salinity and pressure coefficients $\gamma = \frac{\partial \rho}{\partial S}\big|_{p*,T*}$, $\beta = \frac{\partial \rho}{\partial p}\big|_{S*,T*}$ are set to 0.7665 kg m^{-3} ppt^{-1} and 4.55 $\times$ 10^{-7} kg m^{-3} Pa^{-1}, respectively. Using Darcy's law to describe the flow (e.g., Bear 1972), the fluid velocity v can be expressed as a function of material properties and the pressure field:

$$\phi v = -\frac{\kappa}{\mu}\left(\nabla p - \rho \overrightarrow{g}\right) \tag{13}$$

where κ is permeability [L^2], μ is dynamic viscosity, set to 0.001 kg m^{-1} s^{-1}, and g is gravitational acceleration. Combining Eqs. 11 and 13, the governing equation for the evolution of the pressure field becomes:

$$\phi\beta\frac{\partial p}{\partial t} = \nabla \cdot \left(\frac{\kappa\rho}{\mu}\left(\nabla p - \rho \overrightarrow{g}\right)\right) - \phi\gamma\frac{\partial S}{\partial t} \tag{14}$$

Solid phase chemical constituents are considered immobile, and mass conservation is expressed as:

$$\frac{d(1-\phi)C_i}{dt} = (1-\phi)R_i \tag{15}$$

where C_i is the solid mass of species i per volume solid phase and R_i the net rate of production or consumption per volume solid phase. For solutes, one can write:

$$\frac{\partial \phi C_i}{\partial t} = \nabla \cdot (D^* \nabla C_i) - \nabla \cdot (\phi v C_i) + \phi R_i \tag{16}$$

where C_i is the solute concentration of species i in the fluid and the reaction rate R is expressed per volume pore fluid. The diffusion–dispersion tensor, D^* [L^2 T^{-1}] is defined as (Scheidegger 1961):

$$D^*_{ij} = \phi D^m \delta_{ij} + (\alpha_L - \alpha_T)\frac{v_i v_j}{|v|} + \alpha_T |v| \delta_{ij} \tag{17}$$

where D^m is the tortuosity corrected in situ molecular diffusion coefficient, δ_{ij} is the Kronecker symbol, and α_L and α_T are longitudinal and transverse dispersivities [L], respectively.

Implementation

In each time step, the pressure field is solved (14) from which the velocity field is calculated (13). Subsequently, the evolution of the chemical species is computed (15, 16). For solutes, this is accomplished using sequential non-iterative operator splitting (Steefel and MacQuarrie 1996). In this approach, concentrations of all species are first calculated subject to advective and dispersive transport only. Without coupling between species through the reaction term, the temporal evolution for each chemical compound due to transport can be solved individually. The governing equations are discretized using a Galerkin finite element formulation and forward Euler time stepping. The resulting algebraic set of equations is solved using a diagonally preconditioned conjugate gradient solver (Reddy 1993; Meile and Tuncay 2006). The impact of the reactions is then computed by solving a set of coupled, typically stiff, ordinary differential equations for each spatial node, using the public domain solver VODE (Brown et al. 1989) with backward differentiation and the generation of full Jacobian matrix settings. Equilibrium reactions are implemented via operator splitting through mass conserving distribution functions at the end of each time step (e.g., Tadanier and Eick 2002).

The implementation of the reaction network solver has been tested by comparison to simulations with explicit rate formulations and implementations using a fully implicit Newton–Raphson approach (Regnier et al. 1997; Meile 2003). Simulations are performed at grid Peclet numbers <4, and the time step is adapted depending on Courant numbers (<1), and adjusted to resolve large temporal changes in concentrations. The finite element mesh has been produced using the open source software *emc2* (Saltel and Hecht 1995), and post-processing is done with the open-source software *OpenDX* and within the proprietary *MATLAB* environment.

Appendix 2

See Table 3.

Table 3 Reaction network

pr_1	$(CH_2O)_{as}(NH_3)_{bs}+as\,O_2+bs\,H^+ \rightarrow as\,CO_2+bs\,NH_4^+ +as\,H_2O$
$pr_{2,DNF}$	$(CH_2O)_{as}(NH_3)_{bs}+\left(\frac{4as}{5}\right)NO_3^- +\left(\frac{4as}{5}+bs\right)H^+ \rightarrow as\,CO_2+bs\,NH_4^+ +\left(\frac{4as}{10}\right)N_2+\left(\frac{7as}{5}\right)H_2O$
$pr_{2,DNRA}$	$(CH_2O)_{as}(NH_3)_{bs}+\left(\frac{as}{2}\right)NO_3^- +(as+bs)H^+ \rightarrow as\,CO_2+\left(\frac{as}{2}+bs\right)NH_4^+ +\left(\frac{as}{2}\right)H_2O$
pr_3	$(CH_2O)_{as}(NH_3)_{bs}+2as\,MnO_2+(4as+bs)H^+ \rightarrow as\,CO_2+bs\,NH_4^+ +2as\,Mn^{2+}+3as\,H_2O$
pr_4	$(CH_2O)_{as}(NH_3)_{bs}+4as\,Fe(OH)_3+(8as+bs)H^+ \rightarrow as\,CO_2+bs\,NH_4^+ +4as\,Fe^{2+}+11as\,H_2O$
pr_5	$(CH_2O)_{as}(NH_3)_{bs}+\left(\frac{as}{2}\right)SO_4^{2-} +\left(\frac{as}{2}+bs\right)H^+ \rightarrow as\,CO_2+bs\,NH_4^+ +\left(\frac{as}{2}\right)HS^- +as\,H_2O$
pr_6	$(CH_2O)_{as}(NH_3)_{bs}+bs\,H^+ \rightarrow \left(\frac{as}{2}\right)CO_2+\left(\frac{as}{2}\right)CH_4+bs\,NH_4^+$
Secondary reactions	*Mineral precipitation–dissolution reactions*
$Mn^{2+}+0.5O_2+H_2O \rightarrow MnO_2+2H^+$ (sr_1)	$Mn^{2+}+HCO_3^- \leftrightarrow MnCO_3+H^+$ (mr_1)
$Fe^{2+}+0.25O_2+2.5H_2O \rightarrow Fe(OH)_3+2H^+$ (sr_2)	$Fe^{2+}+HCO_3^- \leftrightarrow FeCO_3+H^+$ (mr_2)
$2Fe^{2+}+MnO_2+4H_2O \rightarrow 2Fe(OH)_3+Mn^{2+}+2H^+$ (sr_3)	$Fe^{2+}+HS^- \leftrightarrow FeS+H^+$ (mr_3)
$NH_4^+ +2O_2 \rightarrow NO_3^- +2H^+ +H_2O$ (sr_4)	$Ca^{2+}+HCO_3^- \leftrightarrow CaCO_3+H^+$ (mr_4)
$H_2S+2O_2 \rightarrow SO_4^{2-} +2H^+$ (sr_5)	$Ca^{2+}+SO_4^{2-} +2H_2O \leftrightarrow CaSO_4 \cdot 2H_2O$ (mr_5)
$H_2S+MnO_2+2H^+ \rightarrow Mn^{2+}+S^0+2H_2O$ (sr_6)	*Adsorption reactions*
$H_2S+2Fe(OH)_3+4H^+ \rightarrow 2Fe^{2+}+S^0+6H_2O$ (sr_7)	$NH_{4,DISS}^+ \leftrightarrow NH_{4,ADS}^+$ (K_n)
$FeS+2O_2 \rightarrow Fe^{2+}+SO_4^{2-}$ (sr_8)	
$CH_4+2O_2 \rightarrow CO_2+2H_2O$ (sr_9)	
$CH_4+SO_4^{2-}+2H^+ \rightarrow H_2S+CO_2+2H_2O$ (sr_{10})	

Appendix 3

See Table 4.

Table 4 Model parameters

Parameter	Value	Units	Source
Physical characteristics[a]			
ϕ (porosity)	0.4	$m_f^3\ m_t^{-3}$	Field data
κ (permeability)	3.5×10^{-12}	m^2	6
α_L (longitudinal dispersivity)	0.3	m	7
α_T (transverse dispersivity)	0.03	m	10% of α_L
Δh (head gradient)	0.001	m/m	Field data
Organic matter composition and reactivity			
as (Redfield carbon)	106	–	1
bs (Redfield nitrogen)	16	–	1
k_{DOM}	9.51×10^{-12}	s^{-1}	2, modified[b]
Half saturation constants			
KmO_2	0.02	moles m_f^{-3}	2, 3
$KmNO_3$	0.005	moles m_f^{-3}	2, 3
$KmMnO_2$	0.0875	moles m_s^{-3}	2
$KmFeOH_3$	0.0875	moles m_s^{-3}	2
$KmSO_4$	0.03	moles m_f^{-3}	2
Sorption			
K_n	Dependent on salinity	moles m_s^{-3}/moles m_f^{-3}	This study
Secondary reaction rate constants			
sk1	3.17×10^{-4}	(moles $m_f^{-3})^{-1}\ s^{-1}$	2
sk2	3.17×10^{-4}	(moles $m_f^{-3})^{-1}\ s^{-1}$	2
sk3	3.17×10^{-8}	(moles $m_f^{-3})^{-1}\ s^{-1}$	2
sk4	1.59×10^{-4}	(moles $m_f^{-3})^{-1}\ s^{-1}$	2
sk5	5.07×10^{-5}	(moles $m_f^{-3})^{-1}\ s^{-1}$	2
sk6	6.34×10^{-7}	(moles $m_f^{-3})^{-1}\ s^{-1}$	2
sk7	2.54×10^{-7}	(moles $m_f^{-3})^{-1}\ s^{-1}$	2
sk8	9.51×10^{-6}	(moles $m_f^{-3})^{-1}\ s^{-1}$	2
sk9	3.17×10^{-1}	(moles $m_f^{-3})^{-1}\ s^{-1}$	2
sk10	3.17×10^{-7}	(moles $m_f^{-3})^{-1}\ s^{-1}$	2
Mineral precipitation (mkp) and dissolution (mkd) rate constants			
mk1p	3.17×10^{-9}	moles $m_t^{-3}\ s^{-1}$	2
mk1d	3.17×10^{-12}	s^{-1}	2
mk2p	1.59×10^{-9}	moles $m_t^{-3}\ s^{-1}$	2
mk2d	1.59×10^{-12}	s^{-1}	2
mk3p	1.90×10^{-9}	moles $m_t^{-3}\ s^{-1}$	2
mk3d	3.17×10^{-12}	s^{-1}	2
mk4p	1.90×10^{-9}	moles $m_t^{-3}\ s^{-1}$	2
mk4d	1.59×10^{-11}	s^{-1}	2
mk5p	1.90×10^{-9}	moles $m_t^{-3}\ s^{-1}$	2
mk5d	1.59×10^{-11}	s^{-1}	2

Table 4 continued

Parameter	Value	Units	Source
Solubility constants[c]			
K_1	$10^{-10.41}$	–	4
K_2	$10^{-10.55}$	–	4
K_3	$10^{-2.95}$	–	5
K_4	$10^{-8.48}$	–	4
K_5	$10^{-4.58}$	–	4

Subscripts f, s and t denote fluid, solid and total, respectively

Sources: 1. Redfield (1934); 2. Hunter et al. (1998); 3. Van Cappellen and Wang (1996); 4. Stumm and Morgan (1996); 5. Morse et al. (1987); 6. Schultz and Ruppel (2002); 7. Moltyaner et al. (1993)

[a] Porosity is an average of the measured values (0.2–0.5). The imposed head difference is at the low end of the observed pressure gradient from well 2 and 5, selected based on the comparison of model results to measured salinities

[b] See "Modeling results" section

[c] The solubility constants define the saturation states for $MnCO_3$, $FeCO_3$, FeS, $CaCO_3$ and $CaSO_4$, respectively, as: $\Omega_1 = \frac{a_{Mn^{2+}} \cdot a_{HCO_3^-}}{a_{H^+} \cdot K_1}$, $\Omega_2 = \frac{a_{Fe^{2+}} \cdot a_{HCO_3^-}}{a_{H^+} \cdot K_2}$, $\Omega_3 = \frac{a_{Fe^{2+}} \cdot a_{HS^-}}{a_{H^+} \cdot K_3}$, $\Omega_4 = \frac{a_{Ca^{2+}} \cdot a_{HCO_3^-}}{a_{H^+} \cdot K_4}$, $\Omega_5 = \frac{a_{Ca^{2+}} \cdot a_{SO_4^{2-}}}{K_5}$, where a denote activities

References

An S, Gardner W (2002) Dissimilatory nitrate reduction to ammonium (DNRA) as a nitrogen link, versus denitrification as a sink in a shallow estuary (Laguna Madre/Baffin Bay, Texas). Mar Ecol Prog Ser 237:41–50

An S, Joye S (2001) Enhancement of coupled-denitrification by benthic photosynthesis in shallow estuarine sediments. Limnol Oceanogr 46:62–74

Anderson I, Tobias C, Neikirk B, Wetzel R (1997) Development of a process-based nitrogen mass balance for a Virginia (USA) *Spartina alterniflora* salt marsh: implications for net DIN flux. Mar Ecol Prog Ser 159:13–27

Bear J (1972) Dynamics of fluids in porous media. American Elsevier Publishing Company, Inc., New York

Böhlke J, Harvey J, Voytek M (2004) Reach-scale isotope tracer experiment to quantify denitrification and related processes in a nitrate-rich stream, midcontinent United States. Limnol Oceanogr 49:821–838

Böhlke J, Smith R, Miller D (2006) Ammonium transport and reaction in contaminated groundwater: application of isotope tracers and isotope fractionation studies. Water Resour Res 42:W05411. doi:10.1029/2005WR004349

Brown P, Byrne G, Hindmarsh A (1989) VODE: a variable-coefficient ODE solver. SIAM J Sci Stat Comput 10:1038–1051

Burnett W, Bokuniewicz H, Huettel M, Moore W, Taniguchi M (2003) Groundwater and pore water inputs to the coastal zone. Biogeochemistry 66:3–33

Chalmers A (1997) The ecology of Sapelo Island National Estuarine Research Reserve. NOAA Report NA470R0414, 138 pp

Cline J (1969) Spectrophotometric determination of hydrogen sulfide in natural waters. Limnol Oceanogr 14:454–458

Cotrim da Cunha L, Buitenhuis E, Le Quéré C, Giraud X, Ludwig W (2007) Potential impact of changes in river nutrient supply on global ocean biogeochemistry. Glob Biogeochem Cycles 21. doi:10.1029/2006GB002718

De Jonge V, Boynton W, D'Elia C, Elmgren R, Welsh B (1994) Responses to developments in eutrophication in four different North Atlantic estuarine systems. In: Orth R, Dyer K (eds) Changes in fluxes in estuaries: implications from science to management. Olsen & Olsen, Fredensborg

Fazzolari E, Nicolardot B, Germon J (1998) Simultaneous effects of increasing levels of glucose and oxygen partial pressures on denitrification and dissimilatory nitrate reduction to ammonium in repacked soil cores. Eur J Soil Biol 34:47–52

Froelich P, Klinkhammer G, Bender M, Luedtke N, Heath G, Cullen D, Dauphin P (1979) Early oxidation of organic matter in pelagic sediments of the eastern equatorial Atlantic: suboxic diagenesis. Geochim Cosmochim Acta 43:1075–1090

Gardner W, McCarthy M, An S, Sobolev D, Sell K, Brock D (2006) Nitrogen fixation and dissimilatory nitrate reduction to ammonium (DNRA) support nitrogen dynamics in Texas estuaries. Limnol Oceanogr 51(1, part 2): 558–568

Gould W, McCready G (1982) Denitrification in several soils: inhibition by sulfur anions. Can J Microbiol 28:334–340

Hunter K, Wang H, Van Cappellen P (1998) Kinetic modeling of microbially-driven redox chemistry of subsurface environments: coupling transport, microbial metabolism, and geochemistry. J Hydrol 209:53–80

Jensen K, Cox R (1992) Effects of sulfide and low redox potential on the inhibition of nitrous oxide reduction by acetylene in *Pseudomonas nautical*. FEMS Microbiol Lett 96:13–18

Joye S, Hollibaugh J (1995) Sulfide inhibition of nitrification influences nitrogen regeneration in sediments. Science 270:623–625

Kartal B, Kuypers M, Lavik G, Schalk J, Op den Camp H, Jetten M, Strous M (2007) Anammox bacteria disguised as denitrifiers: nitrate reduction to dinitrogen gas via nitrite and ammonium. Environ Microbiol 9:635–642

Kelly-Gerreyn B, Trimmer M, Hydes D (2001) A diagenetic model discriminating denitrification and dissimilatory nitrate reduction to ammonium in a temperate estuarine sediment. Mar Ecol Prog Ser 220:33–46

Koop-Jakobsen K, Giblin A (2009) Anammox in tidal marsh sediments: the role of salinity, nitrogen loading and marsh vegetation. Estuar Coasts 32:238–245

Kroeger K, Charette M (2008) Nitrogen biogeochemistry of submarine groundwater discharge. Limnol Oceanogr 53:1025–1039

Luff R, Haeckel M, Wallmann K (2001) Robust and fast FORTRAN and MATLAB® libraries to calculate pH distributions in marine systems. Comput Geosci 27:157–169

Mantyla A (1987) Standard seawater comparisons updated. J Phys Oceanogr 17:543–548

Meile C (2003) Heterogeneity, uncertainty and process identification in early diagenesis: new model developments with applications to biological mixing. Dissertation, Utrecht University

Meile C, Tuncay K (2006) Scale dependence of reaction rates in porous media. Adv Water Resour 29:62–71

Moltyaner G, Klukas M, Willis C, Killey R (1993) Numerical simulations of Twin Lake natural gradient tracer tests: a comparison of methods. Water Resour Res 29:3433–3452

Moore W (1976) Sampling ^{228}Ra in the deep ocean. Deep Sea Res 23:647–651

Moore W (1984) Radium isotope measurements using germanium detectors. Nucl Instrum Methods 223:407–411

Moore W (1996) Large groundwater inputs to coastal waters revealed by ^{226}Ra enrichments. Nature 380:612–614

Moore W (1999) The subterranean estuary: a reaction zone of ground water and sea water. Mar Chem 65:111–125

Moore W (2003) Sources and fluxes of submarine groundwater discharge delineated by radium isotopes. Biogeochemistry 66:75–93

Moore W, Krest J, Taylor G, Roggenstein E, Joye S, Lee R (2002) Thermal evidence of water exchange through a coastal aquifer: implications for nutrient fluxes. Geophys Res Lett. doi10:1029/2002GL014923

Moore W, Sarmiento J, Key R (2008) Submarine groundwater discharge revealed by ^{228}Ra distribution in the upper Atlantic Ocean. Nature Geosci. doi:10.1038/ngeo183

Morse J, Morin J (2005) Ammonium interaction with coastal marine sediments: influence of redox conditions on *K**. Mar Chem 95:107–112

Morse J, Millero F, Cornwell J, Rickard D (1987) The chemistry of the hydrogen sulfide and iron sulfide systems in natural waters. Earth Sci Rev 24:1–42

Nixon S, Pilson M (1983) Nitrogen in estuarine and coastal marine ecosystems. In: Carpenter E, Capone D (eds) Nitrogen in the marine environment. Academic Press, New York

Nixon S, Ammerman J, Atkinson L, Berounsky V, Billen G, Boicourt W, Boynton W, Church T, Ditoro D, Elmgren R, Garber J, Giblin A, Jahnke R, Owens N, Pilson M, Seitzinger S (1996) The fate of nitrogen and phosphorus at the land sea margin of the North Atlantic Ocean. Biogeochemistry 35:141–180

Paerl H, Pinckney J, Fear J, Peierls B (1998) Ecosystem responses to internal and watershed organic matter loading: consequences for hypoxia in the eutrophying Neuse River Estuary, North Carolina, USA. Mar Ecol Prog Ser 166:17–25

Persky J (1986) The relations of ground-water quality to housing density, Cape Cod, Massachusetts. USGS Water-Resources Investigations Report 86-4093

Pinckney J, Paerl H, Tester P, Richardson T (2001) The role of nutrient loading and eutrophication in estuarine ecology. Environ Health Perspect 109:699–706

Pomeroy L, Wiegert R (eds) (1981) The ecology of a salt marsh. Springer-Verlag, New York

Porubsky W, Weston N, Joye S (2009) Benthic metabolism and the fate of dissolved inorganic nitrogen in intertidal sediments. Estuar Coast Shelf Sci 83:392–402

Press W, Teukolsky S, Vetterling W, Flannery B (1992) Numerical recipes in Fortran 77, vol 1, 2nd edn. Cambridge University Press, Cambridge

Reddy J (1993) An introduction to the finite element method, 2nd edn. McGraw Hill, Inc., New York

Redfield A (1934) On the proportions of organic derivations in seawater and their relation to the composition of plankton. In: Daniel R (ed) James Johnson memorial volume. University Press of Liverpool, Liverpool

Regnier P, Wollast R, Steefel C (1997) Long-term fluxes of reactive species in macrotidal estuaries: estimates from a fully transient, multicomponent reaction-transport model. Mar Chem 58:127–145

Risgaard-Petersen N, Nielsen L, Rysgaard S, Dalsgaard T, Meyer R (2003) Application of the isotope pairing technique in sediments where anammox and denitrification coexist. Limnol Oceanogr Methods 1:63–73

Rosenfeld J (1979) Ammonium adsorption in nearshore anoxic sediments. Limnol Oceanogr 24:356–364

Rysgaard S, Thastum P, Dalsgaard T, Christensen P, Sloth N (1999) Effects of salinity on NH_4^+ adsorption capacity, nitrification, and denitrification in Danish estuarine sediments. Estuaries 22:21–30

Saltel E, Hecht F (1995) EMC2 Wysiwyg 2D finite elements mesh generator. RT no 188 INRIA

Scheidegger A (1961) General theory of dispersion in porous media. J Geophys Res 66:3273–3278

Schultz G, Ruppel C (2002) Constraints on hydraulic parameters and implications for groundwater flux across the upland-estuary interface. J Hydrol 260:255–269

Seitzinger S, Gardner W, Spratt A (1991) The effect of salinity on ammonium sorption in aquatic sediments: implications for benthic nutrient recycling. Estuaries 14:167–174

Silver W, Herman D, Firestone M (2001) Dissimilatory nitrate reduction to ammonium in upland tropical forest soils. Ecology 82:2410–2416

Smith R, Baumgartner L, Miller D, Repert D, Böhlke J (2006) Assessment of nitrification potential in groundwater using short term, single-well injection experiments. Microb Ecol 51:22–35

Snyder M, Taillefert M, Ruppel C (2004) Redox zonation at the saline-influenced boundaries of a permeable surficial aquifer: effects of physical forcing on the biogeochemical cycling of iron and manganese. J Hydrol 296:164–178

Solorzano L (1969) Determination of ammonia in natural waters by the phenonlhypochlorite method. Limnol Oceanogr 14:799–801

Steefel C, MacQuarrie K (1996) Approaches to modeling of reactive transport in porous media. In: Lichtner P, Steefel C, Oelkers E (eds) Reactive transport in porous media, vol 34. Mineralogical Society of America, Washington, DC

Stookey L (1970) Ferrozine—a new spectrophometric reagent for iron. Anal Chem 42:779–781

Stumm W, Morgan J (1996) Aquatic chemistry: chemical equilibria and rates in natural waters. Wiley, New York

Tadanier C, Eick M (2002) Formulating the charge-distribution multisite surface complexation model using FITEQL. Soil Sci Soc Am J 66:1505–1517

Thamdrup B, Dalsgaard T (2002) Production of N_2 through anaerobic ammonium oxidation coupled to nitrate reduction in marine sediments. Appl Environ Microbiol 68:1312–1328

Tiedje J, Sexton A, Myrold D, Robinson J (1982) Denitrification: ecological niches, competition, and survival. Antonie Leeuwenhoek 48:569–583

Tobias C, Anderson I, Canuel E, Macko S (2001) Nitrogen cycling through a fringing marsh-aquifer ecotone. Mar Ecol Prog Ser 210:25–39

Valiela I, Costa J, Foreman K, Teal J, Howes B, Aubrey D (1990) Transport of groundwater-borne nutrients from watersheds and their effects on coastal waters. Biogeochemistry 10:177–197

Valiela I, Collins G, Kremer J, Lajtha K, Geist M, Seely M, Brawley J, Sham C (1997) Nitrogen loading from coastal watersheds to receiving estuaries: new method and application. Ecol Appl 7:358–380

Van Cappellen P, Wang Y (1996) Cycling of iron and manganese in surface sediments: a general theory for the coupled transport and reaction of carbon, oxygen, nitrogen, sulfur, iron, and manganese. Am J Sci 296:197–243

Vervaet H, Boeckx P, Boko A, Van Cleemput O, Hofman G (2004) The role of gross and net N transformation processes and NH_4^+ and NO_3^- immobilization in controlling the mineral N pool of a temperate mixed deciduous forest soil. Plant Soil 264:349–357

Vitousek P, Mooney H, Lubchenco J, Melillo J (1997) Human domination of Earth's ecosystems. Science 277. doi: 10.1126/science.277.5325.494

Vörösmarty C, Loder T III (1994) Spring-neap tidal contrasts and nutrient dynamics in a marsh-dominated estuary. Estuaries 17:537–551